

Design of a Double-Sided *LCLC*-Compensated Capacitive Power Transfer System With Predesigned Coupler Plate Voltage Stresses

Jing Lian, Xiaohui Qu¹, Senior Member, IEEE, Xi Chen², Senior Member, IEEE,
and Chunting Chris Mi³, Fellow, IEEE

Abstract—A high-performance capacitive power transfer (CPT) system is expected to achieve the load-independent constant output, near-zero reactive power, and soft switching of power switches simultaneously, resulting in a reduced power stage, simple control circuitry, and minimum component ratings. However, a well-compensated CPT system still suffers very-high-voltage stresses among not only the main coupled plates but also the leakage coupled plates due to the small coupling and edge emission, which increases the risk of air breakdown and deteriorate the electromagnetic interference (EMI) issue. To solve this problem, the voltage stresses among such coupler plates should be predesigned at an acceptable level. This article systematically analyzes the characteristics of a double-sided *LCLC*-compensated CPT converter that is proven to have enough design freedom providing predesigned voltage stresses for two kinds of coupled plates. Also, three operating frequencies with load-independent constant current (CC) output and input zero-phase angle (ZPA) are found. Without reactive power in the circuit, a parameter design method is proposed for the double-sided *LCLC*-compensated CPT converter at each frequency to satisfy the desired CC output and the predesigned voltage limitations. In this way, the breakdown and EMI issues can be well mitigated by the intended design, and this method can also be extended to other CPT circuits. Finally, a CPT prototype is built to verify the theoretical analysis with the predesigned voltage stresses among the coupler plates.

Index Terms—Capacitive power transfer (CPT), design freedom, *LCLC* compensation, parameter design, voltage stresses.

I. INTRODUCTION

NOWADAYS, the wireless power transfer technology, including inductive power transfer (IPT) and capacitive

Manuscript received February 5, 2020; revised June 24, 2020 and August 24, 2020; accepted October 1, 2020. Date of publication October 13, 2020; date of current version February 3, 2022. This work was supported in part by the National Natural Science Foundation of China under Grant 52077038, in part by the Natural Science Foundation of Jiangsu Province under Grant BK20181280, and in part by the Fundamental Research Funds for Central Universities of China. Recommended for publication by Associate Editor Khurram K. Afridi. (Corresponding author: Xiaohui Qu.)

Jing Lian and Xiaohui Qu are with the School of Electrical Engineering, Southeast University, Nanjing 210096, China, and also with the Jiangsu Key Laboratory of Smart Grid Technology and Equipment, Nanjing 210096, China (e-mail: xhqu@seu.edu.cn).

Xi Chen is with GEIRI North America, San Jose, CA 95134 USA.

Chunting Chris Mi is with the Department of Electrical and Computer Engineering, San Diego State University, San Diego, CA 92182 USA.

Color versions of one or more of the figures in this article are available online at <https://ieeexplore.ieee.org>.

Digital Object Identifier 10.1109/JESTPE.2020.3030657

power transfer (CPT) techniques, has found many applications due to advantages of convenience, safety, and isolation [1]–[6]. The CPT systems use metal plates as couplers, rather than expensive Litz wires and heavy magnetic cores in IPT converters, which could reduce the cost and weight of the whole system. Also, the power transfer medium of CPT systems, i.e., electric fields, can effectively avoid eddy currents and corresponding losses in the nearby metals [7], [8]. Thus, CPT systems are superior to IPT systems in some applications [9].

The coupled metal plates actually behave as capacitors in the CPT system [10], which generates significant reactive power in the circuit. The large reactive power will increase component ratings and degrade the power transfer capability. Therefore, compensation networks are necessary to improve these performances. Similar to a compensated IPT system [11], a well-compensated CPT system should desirably achieve the following characteristics.

- 1) *Zero Phase Angle (ZPA) Between the Input Voltage and Input Current*: The realization of input ZPA can eliminate the reactive power in the circuit and then minimize the component volt–ampere (VA) ratings. Thus, the power transfer capability can be improved effectively.
- 2) *Soft Switching of the Driver Circuit*: When the input ZPA is permitted, the input impedance can be easily modulated to be from purely resistive to slightly inductive for zero-voltage switching (ZVS) of MOSFETs or slightly capacitive for zero-current switching (ZCS) of IGBTs. Soft switching can further reduce power losses and switching noises.
- 3) *Load-Independent Constant Output*: Constant current (CC) or constant voltage (CV) output is required in many practical applications, such as battery or supercapacitor charging and LED lighting. A single-stage CPT converter is expected to provide the desired load-independent output so that the front-end or back-end dc/dc regulator can be saved.

To satisfy the abovementioned requirements, some compensation circuits in CPT systems have been proposed and analyzed, such as a double-sided *LC* circuit [12], [13], a double-sided *LCLC* circuit [14], [15], and a four-coil

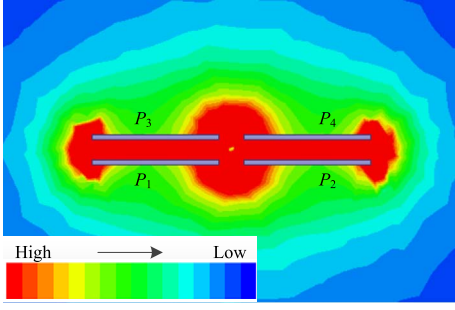


Fig. 1. Electric field emission around the coupler plates, where P_1 and P_2 are placed at the primary side and P_3 and P_4 are placed at the secondary side. P_1 with P_3 and P_2 with P_4 are the main coupled plates, while P_1 with P_2 and P_3 with P_4 are the leakage coupled plates.

compensation circuit [16]. Some circuit design methods are given to improve transfer efficiency [17]–[19]. Unlike the loosely coupled transformer in IPT systems, coupler plates in CPT systems behave like very small coupling capacitances due to the low dielectric coefficient in the air. Therefore, a large amount of electric field emission is released around the plates, especially on the edge of plates, as shown in Fig. 1 [21]. Usually, the plates on the same primary or secondary side are placed closely. From Fig. 1, the edge emission is more serious in the region close to P_1 and P_2 or close to P_3 and P_4 . In this way, there are high-voltage stresses on the main coupling capacitors formed by P_1 and P_3 or P_2 and P_4 and the leakage capacitors formed by P_1 and P_2 or P_3 and P_4 , which can readily exceed the breakdown voltage limitation of 3 kV/mm in the coupler plates [22] and cause a large leakage electric field radiation [23]. To solve the abovementioned issues, prior work [24] tries to maximize the coupling capacitance and then decrease the voltages on the main capacitors. Li *et al.* [16] use resonant networks and an isolated transformer to regulate input and output voltages of coupler plates, and then, the voltages on the main coupled capacitors are decreased. Mai *et al.* [25] reallocate voltage stresses of all compensation components and capacitive couplers by a mathematic calculation based on a double-sided *CL* compensation circuit.

However, the aforementioned works usually optimize the voltage stresses only on the main coupled plates. From Fig. 1, the voltage stresses on the leakage coupled plates are also critical to be optimized [26]. Lian and Qu [27] identify the relationship of voltage stresses between the main coupler plates and the leakage coupler plates based on a simple double-sided *LC*-compensated CPT system. With the desired load-independent CC output and input ZPA, the double-sided *LC*-compensated CPT system has no freedom to optimize such two kinds of voltage stresses. Therefore, a higher order compensation circuit is needed here for the voltage optimization of two kinds of coupled plates.

In this article, a higher order double-sided *LCLC*-compensated CPT converter with enough design freedom is systematically analyzed to fulfill the predesigned voltage stresses among the coupled plates. Meanwhile, three operating frequencies with load-independent CC output and input ZPA are found in Section II. Without reactive power in the circuit,

a parameter design method is proposed to satisfy the required CC output and predesigned voltage stresses for both main coupled plates and leakage coupled plates, as detailed in Section III. This method can be readily extended to the other CPT systems. Finally, a 40-W double-sided *LCLC* CPT system is built, and the experimental results agree well with the theoretical analysis in Section IV. Section V concludes this article.

II. CHARACTERISTIC ANALYSIS FOR INPUT ZPA AND LOAD-INDEPENDENT CONSTANT OUTPUT

Fig. 2 shows the schematic of a double-sided *LCLC*-compensated CPT system where the full-bridge inverter generates the high-frequency ac voltage u_{AB} to power the resonant circuit and two pairs of coupler plates P_1 , P_2 , P_3 , and P_4 . L_{f1} , C_{f1} , L_1 , and C_{ex1} construct the primary *LCLC* network, while L_{f2} , C_{f2} , L_2 , and C_{ex2} construct the secondary *LCLC* network. The structure and dimensions of the coupler are shown in Fig. 3(a) where l is the plate length, d is the air distance, and d_1 is the distance between two plates on the same side. A Π -type model with the equivalent primary capacitor C_P , secondary capacitor C_S , and mutual capacitor C_M can be used in the metal plates, as shown in Fig. 3(b) [28]. The native coupling coefficient k_C is defined as $(C_M/(C_P C_S)^{1/2})$. With C_{ex1} and C_{ex2} parallel to equivalent capacitors $C_P - C_M$ and $C_S - C_M$, respectively, it defines that

$$C_1 = C_{ex1} + C_P \text{ and } C_2 = C_{ex2} + C_S. \quad (1)$$

Then, the equivalent coupling coefficient k becomes

$$k = \frac{C_M}{\sqrt{C_1 C_2}}. \quad (2)$$

And $k < k_C$.

To facilitate the analysis, the double-sided *LCLC*-compensated CPT converter in Fig. 2 can be driven by a purely sinusoidal ac voltage source U_{in} , i.e., the vector of the fundamental component of u_{AB} and delivers power to an equivalent load R_E , as shown in Fig. 4. With the C filter, $R_L = ((\pi^2 R_E)/8)$. Based on the reciprocity principle, Fig. 4 can be further derived as an equivalent T-type network with C_A , C_B , and C_C , as shown in Fig. 5. Here, C_A , C_B , and C_C satisfy

$$\begin{cases} C_A = \frac{C_1 C_2 - C_M^2}{C_2 - C_M} = \frac{C_1(1 - k^2)}{1 - k\sqrt{\frac{C_1}{C_2}}} \\ C_B = \frac{C_1 C_2 - C_M^2}{C_M} = \frac{1 - k^2}{k^2} C_M \\ C_C = \frac{C_1 C_2 - C_M^2}{C_1 - C_M} = \frac{C_2(1 - k^2)}{1 - k\sqrt{\frac{C_2}{C_1}}} \end{cases} \quad (3)$$

A. One Frequency for Input ZPA and Load-Independent Output

From Fig. 5, the primary compensation inductor L_1 can be divided into three parts in series, i.e., L_{11} , L_{12} , and L_{13} , while the secondary L_2 can be divided as L_{21} , L_{22} , and L_{13}

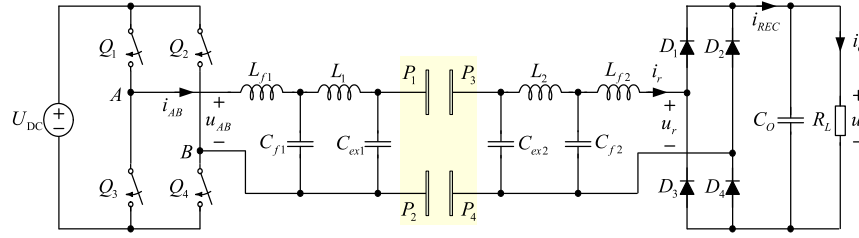


Fig. 2. Schematic of a double-sided *LCLC*-compensated CPT converter.

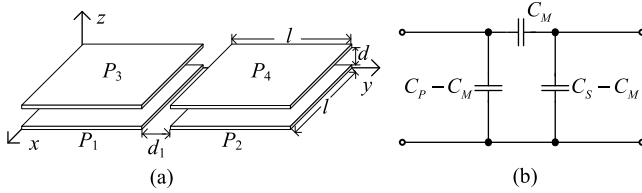


Fig. 3. Coupler structure and equivalent circuit model in the shadow area of Fig. 2. (a) Structure of the coupler. (b) Equivalent II-type model.

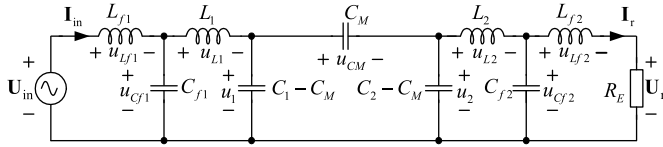


Fig. 4. Equivalent circuit of double-sided *LCLC*-compensated CPT circuit using the II-type model.

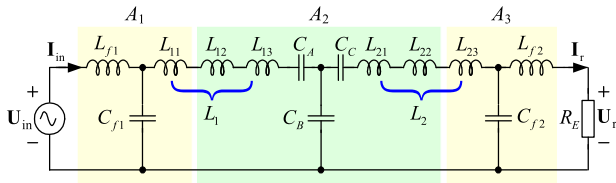


Fig. 5. Equivalent circuit of double-sided *LCLC*-compensated CPT circuit using the T-type model. Each shadow denotes a T network.

in series. Then, three T networks are given in different color shadows. To find a working angular frequency ω_0 for the CPT converter having properties of input ZPA and load-independent output, every T network should satisfy $Z_1 = -Z_2 = Z_3$ at ω_0 in Fig. 6 where

$$\begin{aligned} \omega_0 &= \frac{1}{\sqrt{L_{f1}C_{f1}}} = \frac{1}{\sqrt{L_{f2}C_{f2}}} \\ &= \frac{1}{\sqrt{L_{11}C_{f1}}} = \frac{1}{\sqrt{L_{12}C_B}} = \frac{1}{\sqrt{L_{13}C_A}} \\ &= \frac{1}{\sqrt{L_{23}C_{f2}}} = \frac{1}{\sqrt{L_{22}C_B}} = \frac{1}{\sqrt{L_{21}C_C}}. \end{aligned} \quad (4)$$

Then, the output current I_{r1} and the input impedance Z_{IN1} at ω_0 are given by

$$I_{r1} = j \frac{\omega_0 k^2 C_{f1} C_{f2} U_{in}}{(1 - k^2) C_M} \quad (5)$$

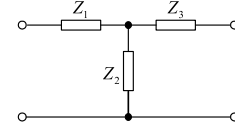


Fig. 6. Typical T network.

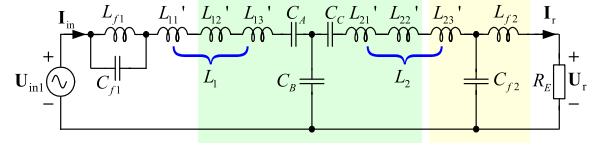


Fig. 7. Equivalent circuit of Fig. 5 operating at ω_1 , not ω_0 .

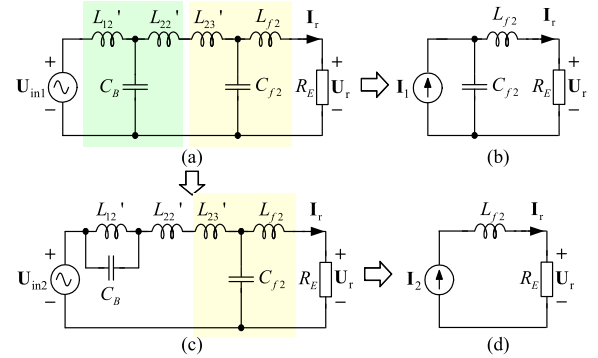


Fig. 8. (a)–(d) Derivation circuits of Fig. 7.

and

$$Z_{IN1} = \frac{1}{R_E} \left[\frac{C_M}{\omega_0 C_{f1} C_{f2}} \left(\frac{1}{k^2} - 1 \right) \right]^2. \quad (6)$$

A load-independent CC output and input ZPA are realized at ω_0 that is consistent with the result in [14].

B. Other ZPA Frequencies for Load-Independent Output

With the parameter constraints in (4), the CPT converter may not work at ω_0 but at another frequency ω_1 . Then, the equivalent circuit in Fig. 5 can be transformed as that in Fig. 7 by Thevenin's theorem. The primary L_1 can still be divided into three parts, i.e., L'_{11} , L'_{12} , and L'_{13} , and the secondary L_2 is divided as L'_{21} , L'_{22} , and L'_{23} . If L'_{11} is designed to resonate with L_{f1} paralleled by C_{f1} at ω_1 , a load-independent voltage source U_{in1} drives the following circuit, as shown in Fig. 8(a). Designing that L'_{13} resonates with

C_A while L'_{21} resonates with C_C , Fig. 8(a) has two typical T networks. There are two cases for further derivation, which are as follows.

- 1) If L'_{12} resonates with C_B at ω_1 , \mathbf{U}_{in1} can be transformed to a load-independent current source \mathbf{I}_1 , as shown in Fig. 8(b). By (4), L_{f2} cannot resonate with C_{f2} at ω_1 . Thus, it is impossible to realize CC or CV output for R_E in Fig. 8(b).
- 2) If L'_{12} cannot resonate with C_B at ω_1 , Fig. 8(a) can be converted to Fig. 8(c) by Thevenin's theorem with a new load-independent voltage source \mathbf{U}_{in2} in series with the parallel connection of L'_{12} and $(1/(j\omega_1 C_B))$. Design that L'_{22} resonates with L'_{12} paralleled by C_B while L'_{23} resonates with C_{f2} . Then, a load-independent current \mathbf{I}_2 can drive the load R_E directly, as shown in Fig. 8(d).

Following the abovementioned analysis, we have:

$$\begin{aligned}\omega_1 &= \sqrt{\frac{L_{f1} + L'_{11}}{L'_{11}L_{f1}C_{f1}}} = \sqrt{\frac{L'_{12} + L'_{22}}{L'_{12}L'_{22}C_B}} \\ &= \frac{1}{\sqrt{L'_{13}C_A}} = \frac{1}{\sqrt{L'_{21}C_C}} = \frac{1}{\sqrt{L'_{23}C_{f2}}}.\end{aligned}\quad (7)$$

Under the constraint of the same set of compensation parameters

$$L_1 = L_{11} + L_{12} + L_{13} = L'_{11} + L'_{12} + L'_{13}$$

and

$$L_2 = L_{21} + L_{22} + L_{23} = L'_{21} + L'_{22} + L'_{23}.\quad (8)$$

Substituting (4) and (7) into (8), we have (9), as shown at the bottom of the page.

Although a new load-independent CC output can be found at ω_1 in Fig. 8(d), the input impedance cannot be guaranteed to be resistive. To ensure the input ZPA, a transmission matrix A_T of the CPT system is introduced here, which satisfies

$$\begin{bmatrix} \mathbf{U}_{in} \\ \mathbf{I}_{in} \end{bmatrix} = A_T \begin{bmatrix} \mathbf{U}_r \\ \mathbf{I}_r \end{bmatrix} = \begin{bmatrix} a_{11} & ja_{12} \\ ja_{21} & a_{22} \end{bmatrix} \begin{bmatrix} \mathbf{U}_r \\ \mathbf{I}_r \end{bmatrix}.\quad (10)$$

The CPT converter can still be divided into three T networks with matrixes A_1 , A_2 , and A_3 , as shown in Fig. 5, where $L_{11,12,13,21,22,23}$ should be $L'_{11,12,13,21,22,23}$. By the basic theory of two-port network

$$A_T = A_1 A_2 A_3 = \begin{bmatrix} a'_{11} & a'_{12} \\ a'_{13} & a'_{14} \end{bmatrix} \begin{bmatrix} a'_{21} & a'_{22} \\ a'_{23} & a'_{24} \end{bmatrix} \begin{bmatrix} a'_{31} & a'_{32} \\ a'_{33} & a'_{34} \end{bmatrix}.\quad (11)$$

Matrixes A_1 , A_2 , and A_3 are given by

$$\begin{aligned}A_1 &= \begin{bmatrix} 1 - \omega_1^2 L_{f1} C_{f1} & 0 \\ j\omega_1 C_{f1} & 1 - \omega_1^2 L'_{11} C_{f1} \end{bmatrix} \\ A_2 &= \begin{bmatrix} 1 - \omega_1^2 L'_{12} C_B & 0 \\ j\omega_1 C_B & 1 - \omega_1^2 L'_{22} C_B \end{bmatrix}\end{aligned}$$

and

$$A_3 = \begin{bmatrix} 0 & j\omega_1 L'_{23} \\ j\omega_1 C_{f2} & 1 - \omega_1^2 L_{f2} C_{f2} \end{bmatrix}.\quad (12)$$

By solving (11) and (12), $a_{11} = a'_{31}(a'_{11}a'_{21} + a'_{12}a'_{23}) + a'_{33}(a'_{11}a'_{22} + a'_{12}a'_{24}) = 0$. Then, the input impedance of the CPT circuit can be expressed as

$$Z_{IN} = \frac{\mathbf{U}_{in}}{\mathbf{I}_{in}} = \frac{ja_{12}}{a_{22} + ja_{21}R_E} = \frac{a_{21}a_{12}R_E + ja_{12}a_{22}}{a_{22}^2 + a_{21}^2 R_E^2}.\quad (13)$$

If Z_{IN} is purely resistive, $a_{12}a_{22} = 0$ from (13). If $a_{12} = 0$, the input impedance is always zero, which is not practical. Therefore, $a_{22} = 0$. By (11)

$$\begin{aligned}a_{22} &= a'_{32}(a'_{13}a'_{21} + a'_{14}a'_{23}) + a'_{14}a'_{24}a'_{34} \\ &= (C_{f1}C_2 - C_1C_{f2})\frac{\omega_1^2 - \omega_0^2}{C_M C_{f2}\omega_0^2} = 0.\end{aligned}\quad (14)$$

Thus, a ZPA design constraint is obtained as

$$C_{f1}C_2 - C_1C_{f2} = 0.\quad (15)$$

Substituting (15) into (9), the other two frequencies $\omega_{1H,1L}$ with input ZPA and load-independent CC output can be given as

$$\omega_{1H} = \omega_0\sqrt{1 + \alpha} \quad \text{and} \quad \omega_{1L} = \omega_0\sqrt{1 - \alpha}\quad (16)$$

where $\alpha = (((1 - k^2)^2(C_2/C_{f2})^2 + (C_2/C_{f2})(1 - k^2) + k^2)^{1/2})/(1 + (1 - k^2)(C_2/C_{f2}))$.

The load-independent CC current \mathbf{I}_2 and the input impedance Z_{IN2} at ω_{1H} and ω_{1L} are identical and given by

$$\mathbf{I}_2 = -j\frac{\omega_1 C_M}{k^2} \left(1 - k^2 + \frac{1}{\beta}\right) \mathbf{U}_{in}\quad (17)$$

and

$$Z_{IN2} = \frac{k^4 \beta^2}{[(1 - k^2)\beta + 1]^2 \omega_1^2 C_M^2 R_E}\quad (18)$$

where $\beta = (C_1/C_{f1}) = (C_2/C_{f2})$.

In summary, with so many compensation components, i.e., $C_{f1,f2}$, $L_{f1,f2}$, $C_{1,2}$, and $L_{1,2}$, the double-sided *LCLC*-compensated CPT converter has three ZPA frequencies with load-independent CC output and may have enough design freedom to optimize the voltage stresses among coupler plates, which will be analyzed in Section III.

III. DESIGN AND IMPLEMENTATION OF CPT CONVERTER WITH VOLTAGE STRESS OPTIMIZATION

A. Design Freedom and Optimization Theory

As analyzed in Section II, the double-sided *LCLC*-compensated CPT converter can be designed at ω_0 or ω_1 to realize input ZPA and output load-independent

$$\omega_1 = \omega_0 \sqrt{1 \pm \sqrt{\frac{1 + \left(\frac{1}{k^2} - 1\right) \frac{C_1}{C_{f1}} + \left(\frac{1}{k^2} - 1\right)^2 \frac{C_M^2}{C_{f1}C_{f2}}}{\frac{1}{k^2} + \left(\frac{1}{k^2} - 1\right) \left(\frac{C_1}{C_{f1}} + \frac{C_2}{C_{f2}}\right) + \left(\frac{1}{k^2} - 1\right)^2 \frac{C_M^2}{C_{f1}C_{f2}}}}}\quad (9)$$

CC. As shown in Fig. 2, the input dc voltage U_{dc} can be modulated by $Q_{1,2,3,4}$ with D being the duty cycle of u_{AB} in one half cycle. The fundamental component of u_{AB} , denoted as u_{IN} , is given as

$$u_{IN}(t) = \frac{4U_{dc}}{\pi} \sin \frac{\pi D}{2} \sin \omega t. \quad (19)$$

By (5) and (17), the output current I_{O1} at ω_0 and I_{O2} at ω_1 under C filter should be given as

$$\begin{cases} I_{O1} = \frac{8}{\pi^2} \frac{\omega_0 k^2 C_{f1} C_{f2}}{C_M(1-k^2)} U_{dc} \sin \frac{\pi D}{2} \\ I_{O2} = \frac{8}{\pi^2} \frac{\omega_1 C_M}{k^2} \left(1 - k^2 + \frac{C_{f2}}{C_2}\right) U_{dc} \sin \frac{\pi D}{2}. \end{cases} \quad (20)$$

From (20), with the given U_{dc} , coupler parameter C_M , and operating frequency, both I_{O1} and I_{O2} are functions of C_{f1} , C_{f2} , C_1 , and C_2 . Meanwhile, it should be noticed that L_{f1} , L_{f2} , L_1 , and L_2 are also the functions of C_{f1} , C_{f2} , C_1 , and C_2 by (4) and (7). Therefore, with one constraint of (20), the double-sided *LCLC*-compensated CPT converter has the design freedom to optimize u_{CM} , u_1 , and u_2 with four independent control variables: C_{f1} , C_{f2} , C_1 , and C_2 . It is the reason why the low-order compensation circuit cannot optimize all voltages among the coupler plates. For example, the double-sided *LC*-compensated CPT converter only has two independent variables C_1 and C_2 so that voltage stresses of u_1 and u_2 cannot be designed below the given values in [27].

For any CPT system, the key coupler plates can be modeled as a Π -type network, as shown in Fig. 4. Assuming that all reactive components are lossless, the transferred real power P of the CPT converter is actually the power transferred via the Π -type network. Therefore, we have

$$\begin{cases} P = \frac{1}{2} \omega C_M U_1 U_2 \sin \varphi \\ U_{CM}^2 = U_1^2 + U_2^2 - 2U_1 U_2 \cos \varphi \geq 2U^2(1 - \cos \varphi) \end{cases} \quad (21)$$

where $P = I_O^2 R_L$, $U_{1,2}$ is the magnitude of $u_{1,2}$, and φ is the phase angle between u_1 and u_2 . The minimum U_{CM} occurs when $U_1 = U_2 = U$. By solving (21), it can be written as

$$U_{CM} = \sqrt{2}U \sqrt{1 \pm \sqrt{1 - \left(\frac{2P}{\omega C_M U^2}\right)^2}} \quad (22)$$

where \pm is decided by φ with $-$ for $[-(\pi/2), (\pi/2)]$ and $+$ for $[-\pi, -(\pi/2)]$ or $[(\pi/2), \pi]$ in one period. If (22) makes sense

$$\omega \geq \frac{2P}{C_M U^2} \geq \frac{2P}{C_M U_{\max}^2} \quad (23)$$

where U_{\max} is the given maximum voltage of u_1 or u_2 . Besides, the maximum voltage $U_{CM\max}$ of u_{CM} is usually given to avoid the air breakdown and electromagnetic interference (EMI) issue. From (22), with the given output power P , coupler parameter C_M , U_{\max} , and $U_{CM\max}$, the operating frequency ω should be considered carefully besides the constraint of (23).

With the abovementioned consideration, (22) can be rewritten as

$$\omega = \frac{4P}{C_M U_{CM} \sqrt{4U^2 - U_{CM}^2}}. \quad (24)$$

The relationship of ω to U and U_{CM} can be judged by

$$\frac{\partial \omega}{\partial U} = -\frac{16PU}{C_M U_{CM} (\sqrt{4U^2 - U_{CM}^2})^3} \quad (25)$$

and

$$\frac{\partial \omega}{\partial U_{CM}} = \frac{8P(U_{CM}^2 - 2U^2)}{C_M U_{CM}^2 (\sqrt{4U^2 - U_{CM}^2})^3}. \quad (26)$$

According to (25) and (26), $(\partial \omega / \partial U) < 0$, while $(\partial \omega / \partial U_{CM})$ depends on the relationship between U_{CM} and $\sqrt{2}U$.

- 1) If $\varphi \in [-(\pi/2), (\pi/2)]$, $U_{CM} < \sqrt{2}U$ in (22). From (26), $(\partial \omega / \partial U_{CM}) < 0$. Therefore, with the given U_{\max} and $U_{CM\max}$, the minimum ω can be readily determined by

$$\omega \geq \frac{4P}{C_M U_{CM\max} \sqrt{4U_{\max}^2 - U_{CM\max}^2}}. \quad (27)$$

- 2) If $\varphi \in [-\pi, -(\pi/2)]$ or $[(\pi/2), \pi]$, $U_{CM} > \sqrt{2}U$. From (26), $(\partial \omega / \partial U_{CM}) > 0$. It is hard to determine a minimum ω by (24). Thus, we should check the relationship between U_{CM} and U . From (22) with $+$, it is evident that $(\partial U_{CM} / \partial U) > 0$, and then, we have $U_{CM} \geq \sqrt{2}U$. Substitute $U \geq (2P / \omega C_M)^{1/2}$ by (23) into $U_{CM} \geq \sqrt{2}U$, and we have

$$\omega \geq \frac{4P}{C_M U_{CM}^2} \geq \frac{4P}{C_M U_{CM\max}^2}. \quad (28)$$

Summarily, for any CPT converter with enough independent variables, the operating angular frequency ω can be designed by (23) and (27) for $\varphi \in [-(\pi/2), (\pi/2)]$ or by (23) and (28) for $\varphi \in [-\pi, -(\pi/2)]$ or $[(\pi/2), \pi]$, satisfying the requirement of output power, given coupler plates and given coupler plate voltage stresses. The range of φ should be analyzed for the detailed CPT topology.

B. Phase Angle for Different Angular Frequencies

The phase angle φ between u_1 and u_2 for a double-sided *LCLC*-compensated CPT converter, as shown in Fig. 2, can be determined by the expressions of vectors \mathbf{U}_1 and \mathbf{U}_2 , as given in (29), at ω_0 and (30) at ω_1 , i.e., $\omega_{1H,1L}$

$$\begin{cases} \mathbf{U}_1|_{\omega_0} = \left(1 - \frac{L_1}{L_{f1}} + \frac{1}{j\omega_0 C_{f1} Z_{IN1}}\right) \mathbf{U}_{in} \\ \mathbf{U}_2|_{\omega_0} = \left[R_E \left(1 - \frac{L_2}{L_{f2}}\right) - \frac{1}{j\omega_0 C_{f2}}\right] \mathbf{I}_{r1}. \end{cases} \quad (29)$$

From (4), $L_1 > L_{f1}$ and $L_2 > L_{f2}$. From (6), $Z_{IN1} > 0$. Substituting (5) into (29), we have $\Re(\mathbf{U}_1) < 0$, $\Im(\mathbf{U}_1) < 0$, $\Re(\mathbf{U}_2) < 0$, and $\Im(\mathbf{U}_2) < 0$. Thus, both \mathbf{U}_1 and \mathbf{U}_2 are located at the third quadrant at ω_0 , as shown in Fig. 9(a) and (b), where $\varphi \in [-(\pi/2), (\pi/2)]$.

Similarly, if the CPT converter operates at ω_1

$$\begin{cases} \mathbf{U}_1|_{\omega_1} = \left[\gamma - \frac{j\omega_1 L f_1}{Z_{IN2}} \left(\gamma + \frac{\omega_0^2}{\omega_1^2} (1 - \gamma) \right) \right] \mathbf{U}_{in} \\ \mathbf{U}_2|_{\omega_1} = \left[\gamma R_E + j\omega_1 L f_2 \left(\gamma + \frac{\omega_0^2}{\omega_1^2} (1 - \gamma) \right) \right] \mathbf{I}_{r2} \end{cases} \quad (30)$$

where $\gamma = 1 - (\omega_1^2/\omega_0^2)(1 + (1/((1 - k^2)\beta)))$. If the CPT converter works at ω_{1H} , $(\omega_1^2/\omega_0^2) = 1 + \alpha$ by (16) and $\alpha > 0$. Thus, $\gamma < 0$. The expression of $\gamma + (\omega_0^2/\omega_1^2)(1 - \gamma)$ can be derived to be always negative. From (18), $Z_{IN2} > 0$. Substituting (17) into (30), we have $\Re(\mathbf{U}_1) < 0$, $\Im(\mathbf{U}_1) > 0$, $\Re(\mathbf{U}_2) < 0$, and $\Im(\mathbf{U}_2) > 0$. Then, both \mathbf{U}_1 and \mathbf{U}_2 at ω_{1H} are located at the second quadrant with $\varphi \in [-(\pi/2), (\pi/2)]$, as shown in Fig. 9(c) and (d). If the CPT converter works at ω_{1L} , $(\omega_1^2/\omega_0^2) = 1 - \alpha$. The expression of $\gamma + (\omega_0^2/\omega_1^2)(1 - \gamma)$ can be derived to be always positive. Thus, $\Im(\mathbf{U}_1) < 0$ and $\Re(\mathbf{U}_2) > 0$. However, the polarity of γ cannot be uniquely determined by

$$\gamma|_{\omega_{1L}} = \frac{\sqrt{(1 - k^2)^2 \beta^2 + (1 - k^2)\beta + k^2} - 1}{(1 - k^2)\beta}. \quad (31)$$

There are two cases for γ , which are as follows.

- 1) If $\beta < (((5 - 4k^2)^{1/2} - 1)/(2(1 - k^2)))$, $\gamma < 0$. Then, $\Re(\mathbf{U}_1) < 0$ and $\Im(\mathbf{U}_2) > 0$. Thus, \mathbf{U}_1 is located at the third quadrant, and \mathbf{U}_2 is located at the first quadrant at ω_{1L} , as shown in Fig. 9(e) and (f). Thus, $\varphi \in [-\pi, -(\pi/2)]$ or $[(\pi/2), \pi]$.
- 2) If $\beta > (((5 - 4k^2)^{1/2} - 1)/(2(1 - k^2)))$, $\gamma > 0$. Then, $\Re(\mathbf{U}_1) > 0$ and $\Im(\mathbf{U}_2) < 0$. Thus, \mathbf{U}_1 and \mathbf{U}_2 are both located at the fourth quadrant with $\varphi \in [-(\pi/2), (\pi/2)]$, as shown in Fig. 9(g) and (h).

From Section III-A, in the double-sided *LCLC*-compensated CPT converter, the operating angular frequencies ω_0 and ω_{1H} should be designed by (23) and (27) due to $\varphi \in [-(\pi/2), (\pi/2)]$. The operating angular frequency ω_{1L} can be designed by (23) and (27) for $\varphi \in [-(\pi/2), (\pi/2)]$ or by (23) and (28) for $\varphi \in [-\pi, -(\pi/2)]$ or $[(\pi/2), \pi]$. However, it should be noticed that the operation range of φ is determined by the relationship between β and $(((5 - 4k^2)^{1/2} - 1)/(2(1 - k^2)))$. Therefore, if the CPT converter is designed at ω_{1L} , β and k can be solved by Section III-C, and φ must be rechecked to satisfy the predesigned range.

C. Parameter Design Process

From Section III-B, the phase angle φ of the double-sided *LCLC*-compensated CPT converter has two cases. With the predesigned U_{CMmax} , U_{max} , I_O , C_M , U_{dc} , and full output power P , the operating angular frequencies ω_0 , ω_{1H} , and ω_{1L} can be calculated in a range by (23) and (27) or by (23) and (28). Select ω as the operating angular frequency, and (23) can be rewritten as

$$\sqrt{\frac{2P}{\omega C_M}} \leq U \leq U_{max}. \quad (32)$$

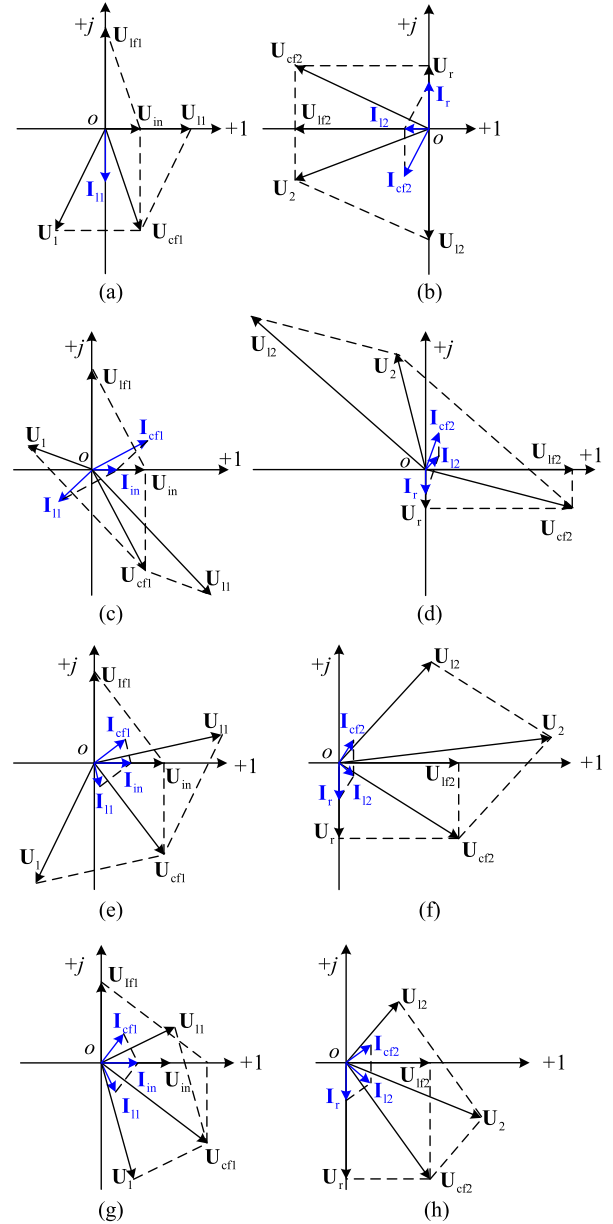


Fig. 9. Vector voltages and currents of the double-sided *LCLC*-compensated CPT converter at (a) and (b) ω_0 , (c) and (d) ω_{1H} , and (e)–(h) ω_{1L} .

Meanwhile, $U_{CM} \leq U_{CMmax}$. With (22), two cases of φ should be considered, which are as follows.

- 1) If $\varphi \in [-(\pi/2), (\pi/2)]$, substitute U_{CMmax} into (22) with $-$ and solve U as U_{solu1} . The relationship between U and U_{CM} can be determined by

$$\frac{\partial U_{CM}}{\partial U} = \frac{\sqrt{2}}{\sqrt{1 - \sqrt{1 - \frac{4P^2}{\omega^2 C_M^2 U^4}}}} \cdot \left(1 - \frac{1}{\sqrt{1 - \frac{4P^2}{\omega^2 C_M^2 U^4}}} \right) < 0. \quad (33)$$

Thus

$$U \geq U_{solu1}. \quad (34)$$

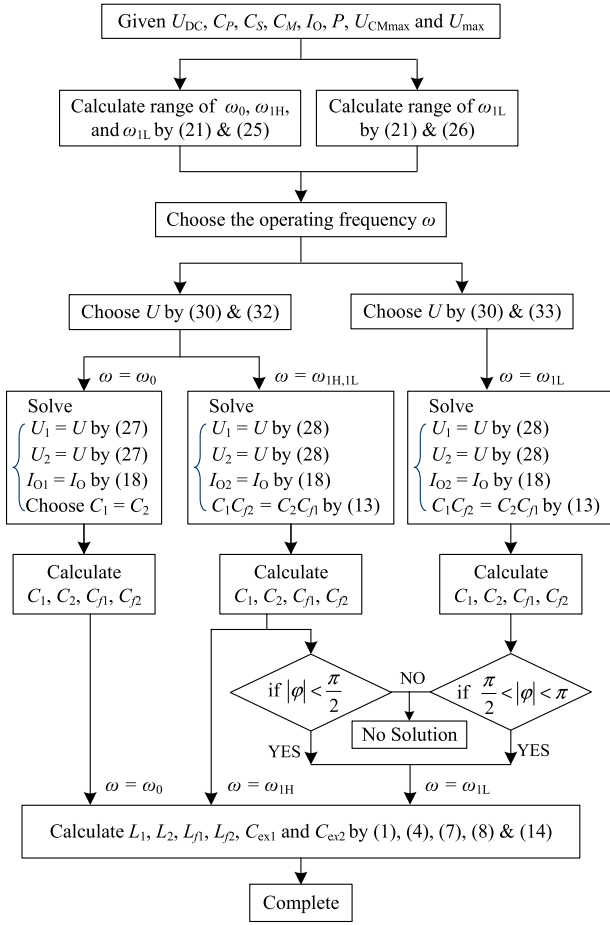


Fig. 10. Parameter design chart of a double-sided *LCLC*-compensated CPT converter.

- 2) If $\varphi \in [-\pi, -(\pi/2)]$ or $[(\pi/2), \pi]$, substitute U_{CMmax} into (22) with + and solve U as U_{solu2} . Due to $(\partial U_{CM}/\partial U) > 0$ at this case

$$U \leq U_{solu2}. \quad (35)$$

From (32) and (34) or (35), U can be selected to guarantee $U_{CM} \leq U_{CMmax}$. Then, we can combine four equations to solve four independent parameters C_{f1} , C_{f2} , C_1 , and C_2 , which includes $U_1 = U_2 = U$ by (29) or (30), $I_O = I_{O1}$, or $I_O = I_{O2}$ by (20) and (15) for ω_1 . Here, it should be noted that there are only three equations for ω_0 case. Therefore, one parameter among C_{f1} , C_{f2} , C_1 , and C_2 can be predesigned, for example, $C_1 = C_2$. The detailed design process is given in Fig. 10. From Fig. 10, φ must satisfy one case of $|\varphi| < (\pi/2)$ or $(\pi/2) < |\varphi| < \pi$ at least. Thus, if one case is not satisfied, there is no solution, and φ can satisfy the other case to find the solution. The operating frequency could be selected according to the requirements of applications, product volume, cost, efficiency, and EMI issues.

D. Soft Switching Realization

Fig. 11 shows the normalized output current and phase angle versus normalized parameters at ω_0 , ω_{1H} , and ω_{1L} , respectively. From Fig. 11(a) and (b), it can be seen that

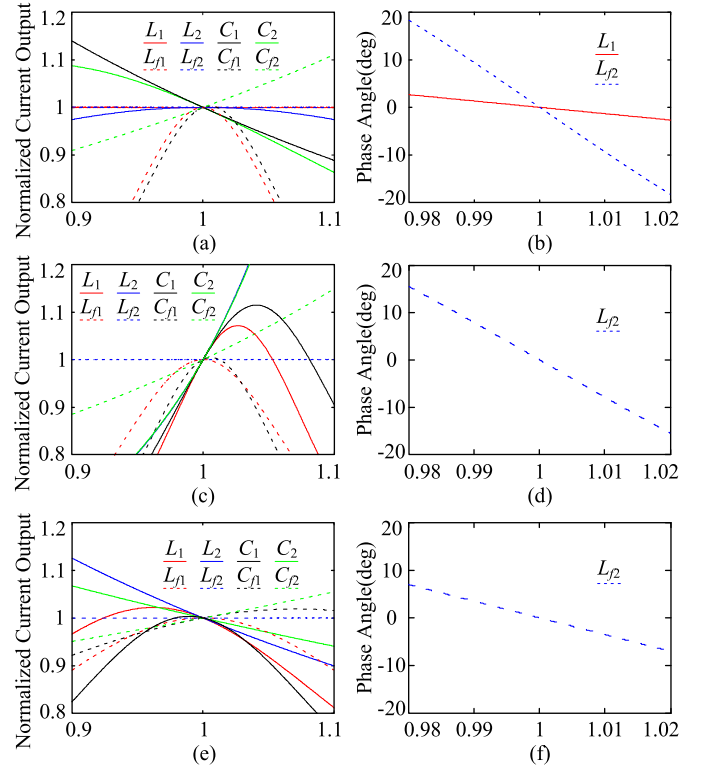


Fig. 11. Normalized output current and phase angle versus normalized parameters at (a) and (b) ω_0 , (c) and (d) ω_{1H} , and (e) and (f) ω_{1L} .

the output current is not sensitive to L_1 and L_{f2} variations at ω_0 . Then, the smaller L_1 and L_{f2} will permit the ZVS of CPT converters, which is consistent with the results in [15]. Similarly, the output current is not sensitive to the variation of L_{f2} at both ω_{1H} and ω_{1L} from Fig. 11(c) and (e). A small decrement of L_{f2} can ensure ZVS from Fig. 11(d) and (f).

IV. EXPERIMENT VERIFICATION

To verify the abovementioned analysis, a 40-W double-sided *LCLC*-compensated CPT prototype is built to provide a CC of 2 A, as shown in Fig. 12. The length l of each coupler plate is 200 mm, and the air distance d is 6 mm. The distance d_1 between two plates on the same primary or secondary side is 10 mm. The equivalent parameters can be measured as $C_M = 35$ pF and $C_P = C_S = 40$ pF. The input dc voltage is 24 V, and the duty cycle is set as 0.95. The predesigned maximum voltage stress U_{CMmax} is 800 V, and U_{max} is 1200 V.

From Fig. 10, the operating frequency can be calculated as $f \geq 402$ kHz for f_0 , $f_{1H,1L}$, and $\varphi \in [-(\pi/2), (\pi/2)]$, while $f \geq 1.14$ MHz for f_{1L} and $\varphi \in [-\pi, -(\pi/2)]$ or $[(\pi/2), \pi]$. If f is designed at 500 kHz as f_0 and $f_{1H,1L}$ for $\varphi \in [-(\pi/2), (\pi/2)]$, the calculated U belongs to [994 V, 1200 V] and U_{CM} belongs to [629 V, 800 V]. If f is designed as 1.5 MHz as f_{1L} for $\varphi \in [-\pi, -(\pi/2)]$ or $[(\pi/2), \pi]$, U belongs to [493 V, 502 V] and U_{CM} belongs to [697 V, 800 V]. We choose $U_{CM} = 750$ V with a design margin, and the calculated U , $C_{f1,2}$, $C_{ex1,2}$, $L_{1,2}$, and $L_{f1,2}$ are given in Table I. It should be noted there is no solution for f_{1L} when $\varphi \in [-(\pi/2), (\pi/2)]$. The CPT converter can be designed to

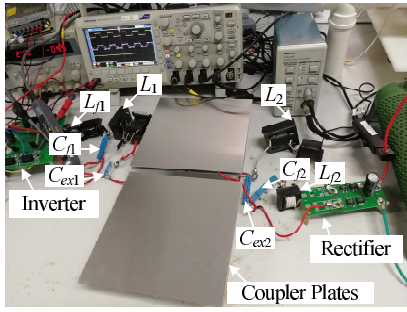


Fig. 12. Experimental prototype of the double-sided *LCLC*-compensated CPT converter.

TABLE I

CALCULATED PARAMETERS FOR CPT CONVERTER AT DIFFERENT FREQUENCIES UNDER U_{CM} OF 750 V

Parameter	$f_0 = 500$ kHz	$f_{1H} = 500$ kHz	$f_{1L} = 1.5$ MHz
U	1041 V	1041 V	495 V
C_{f1}	1.98 nF	3.18 nF	0.92 nF
C_{f2}	2.73 nF	3.69 nF	1.1 nF
C_{ex1}	44 pF	251 pF	234 pF
C_{ex2}	44 pF	296 pF	287 pF
L_{f1}	51.25 μ H	41.52 μ H	6.3 μ H
L_{f2}	42.71 μ H	35.85 μ H	5.3 μ H
L_1	1647 μ H	510 μ H	28.4 μ H
L_2	1638 μ H	441 μ H	23.7 μ H

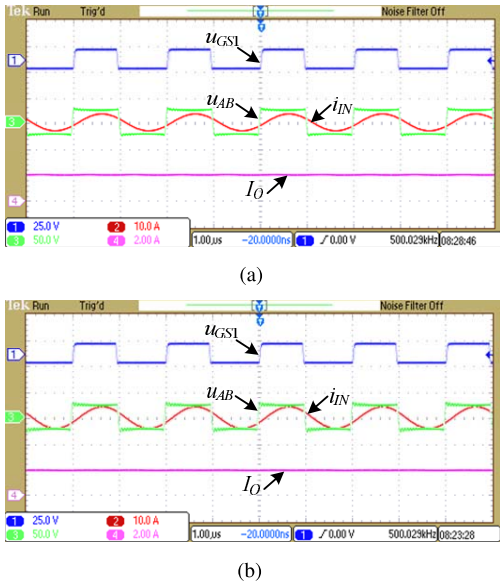


Fig. 13. Experimental waveforms of u_{GS1} , u_{AB} , i_{IN} , and I_O at (a) half load and (b) full load.

work at f_0 or f_{1H} of 500 kHz in the consideration of the implementation of the inverter, efficiency, and EMI issues [29]. Comparing the inductor sizes at two frequencies listed in Table I, f_{1H} of 500 kHz is used here. A microcontroller TMS320F28335 and the gate driver 1EDI20N12AF are used to drive $Q_{1,2,3,4}$. $Q_{1,2,3,4}$ use IPA180N10N3, while the secondary rectifier diodes $D_{1,2,3,4}$ use VB30100S.

Fig. 13 shows the experimental waveforms of gate-source voltage u_{GS1} for MOSFET Q_1 , modulated voltage u_{AB} , input current i_{IN} , and output current I_O for half load of $R_L = 5 \Omega$

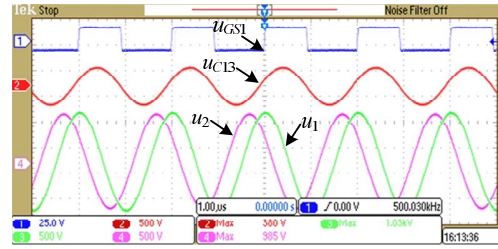


Fig. 14. Experimental waveforms of u_{GS1} , u_{C13} , u_1 , and u_2 at full load.

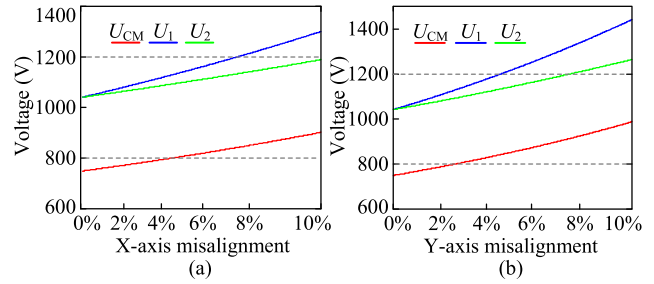


Fig. 15. Voltages U_{CM} , U_1 , and U_2 under (a) *X*-axis misalignment and (b) *Y*-axis misalignment.

and full load of $R_L = 10 \Omega$. It is found that the output current keeps at the required 2 A independent of the load. The small phase angle of i_{IN} lagging u_{AB} facilitates ZVS of the full-bridge switches. To verify the voltage stress optimization, voltage waveforms of u_{GS1} , u_{C13} , u_1 , and u_2 at full load are given in Fig. 14. From Fig. 14, the measured U_1 and U_2 are 1030 and 985 V, which are close to the theoretical values, and the small difference is caused by the capacitor tolerance. U_{C13} is measured as 380 V, where $U_{CM} \approx 2 U_{C13}$, which is also consistent with the value in Table I. The experimental results show good agreement with the calculated values. If the plate misalignment happens, the secondary plates of P_3 and P_4 may move in the *X*-axis or *Y*-axis direction, as shown in Fig. 3(a). Fig. 15 gives the maximum voltage variations of the calculated U_{CM} (i.e., $2U_{C13}$), U_1 , and U_2 under the *X*-axis and *Y*-axis misalignment percentages to the plate length. It can be seen that a small misalignment for the *X*-axis or *Y*-axis is permitted with the predesigned voltage stresses. The efficiency of the CPT converter is measured around 83% at full load, and the losses mainly distribute in the coupler plates, magnetic inductors, and rectifier diodes, which is not the key and omitted in this article.

To further show the electric field emission reduction with the proposed design method, Fig. 16(a) gives the voltage waveforms of u_{C13} , u_1 , and u_2 at the same output current and full load for the double-sided *LCLC* CPT circuit using conventional symmetric parameters, i.e., $C_{ex1} = C_{ex2} = 145$ pF, $C_{f1} = C_{f2} = 6$ nF, $L_1 = L_2 = 731 \mu$ H, and $L_{f1} = L_{f2} = 21 \mu$ H. Compared with Fig. 16(b) with the proposed parameter design, the voltage stresses of U_1 and U_2 are much larger although U_{C13} decreases. Thus, the electric field emissions around the coupler plates are much larger than those in the proposed design, as shown in Fig. 17.

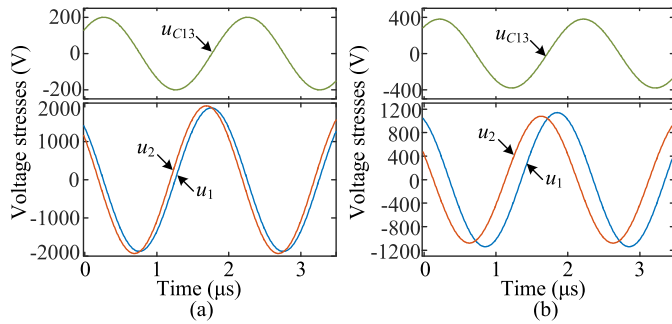


Fig. 16. Comparison of u_{C13} , u_1 , and u_2 at full load with (a) conventional symmetric parameters and (b) proposed parameters in a double-sided $LCLC$ -compensated CPT converter.

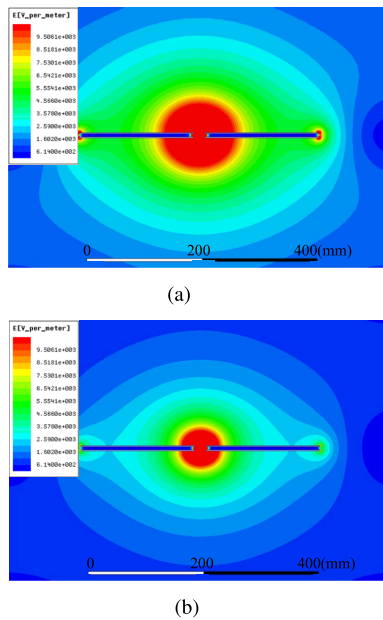


Fig. 17. Electric field emissions around the coupler plates at two cases of parameter design. (a) With conventional symmetric parameters. (b) With proposed parameters.

V. CONCLUSION

To reduce the risk of air breakdown and mitigate the EMI issue in a CPT system, the voltage stresses among both the main coupled plates and the leakage coupled plates should be optimized to the acceptable levels. In this article, a double-sided $LCLC$ -compensated CPT circuit is proven to have enough design freedom to optimize the voltage stresses among the coupler. Meanwhile, three frequencies are found in the double-sided $LCLC$ -compensated CPT circuit to realize input ZPA and load-independent CC output simultaneously, which can facilitate a reduced power stage, simple control circuitry, and high transfer efficiency. Also, a parameter design method is proposed to realize the required load-independent CC output and the predesigned voltage stresses at each frequency. The method can be readily extended to the other CPT systems. Experimental results have validated the theoretical analysis well.

REFERENCES

- [1] S. Samanta and A. K. Rathore, "A new inductive power transfer topology using direct AC-AC converter with active source current waveshaping," *IEEE Trans. Power Electron.*, vol. 33, no. 7, pp. 5565–5577, Jul. 2018.
- [2] M. Lu and K. D. T. Ngo, "Systematic design of coils in series-series inductive power transfer for power transferability and efficiency," *IEEE Trans. Power Electron.*, vol. 33, no. 4, pp. 3333–3345, Apr. 2018.
- [3] D. C. Ludois, J. K. Reed, and K. Hanson, "Capacitive power transfer for rotor field current in synchronous machines," *IEEE Trans. Power Electron.*, vol. 27, no. 11, pp. 4638–4645, Nov. 2012.
- [4] J. Dai and D. C. Ludois, "Single active switch power electronics for kilowatt scale capacitive power transfer," *IEEE J. Emerg. Sel. Topics Power Electron.*, vol. 3, no. 1, pp. 315–323, Mar. 2015.
- [5] Z. Zhang, H. Pang, A. Georgiadis, and C. Cecati, "Wireless power transfer—an overview," *IEEE Trans. Ind. Electron.*, vol. 66, no. 2, pp. 1044–1058, Feb. 2019.
- [6] Y. Chen, Z. Kou, Y. Zhang, Z. He, R. Mai, and G. Cao, "Hybrid topology with configurable charge current and charge voltage output-based WPT charger for massive electric bicycles," *IEEE J. Emerg. Sel. Topics Power Electron.*, vol. 6, no. 3, pp. 1581–1594, Sep. 2018.
- [7] H. Zhang, F. Lu, H. Hofmann, W. Liu, and C. C. Mi, "Six-plate capacitive coupler to reduce electric field emission in large air-gap capacitive power transfer," *IEEE Trans. Power Electron.*, vol. 33, no. 1, pp. 665–675, Jan. 2018.
- [8] J. Dai and D. C. Ludois, "A survey of wireless power transfer and a critical comparison of inductive and capacitive coupling for small gap applications," *IEEE Trans. Power Electron.*, vol. 30, no. 11, pp. 6017–6029, Nov. 2015.
- [9] R. H. W. Liang, C. K. Lee, and S. Y. R. Hui, "Design, analysis and experimental verification of a ball-joint structure with constant coupling for capacitive wireless power transfer," *IEEE J. Emerg. Sel. Topics Power Electron.*, early access, Aug. 29, 2019, doi: 10.1109/JESTPE.2019.2938226.
- [10] C. Liu, A. P. Hu, and N. K. C. Nair, "Modelling and analysis of a capacitively coupled contactless power transfer system," *IET Power Electron.*, vol. 4, no. 7, pp. 808–815, Aug. 2011.
- [11] J. Hou, Q. Chen, Z. Zhang, S.-C. Wong, and C. K. Tse, "Analysis of output current characteristics for higher order primary compensation in inductive power transfer systems," *IEEE Trans. Power Electron.*, vol. 33, no. 8, pp. 6807–6821, Aug. 2018.
- [12] F. Lu, H. Zhang, H. Hofmann, and C. C. Mi, "A double-sided LC-compensation circuit for loosely coupled capacitive power transfer," *IEEE Trans. Power Electron.*, vol. 33, no. 2, pp. 1633–1643, Feb. 2018.
- [13] X.-D. Qing, Z.-H. Wang, Y.-G. Su, Y.-M. Zhao, and X.-Y. Wu, "Parameter design method with constant output voltage characteristic for bilateral LC-compensated CPT system," *IEEE J. Emerg. Sel. Topics Power Electron.*, vol. 8, no. 3, pp. 2707–2715, Sep. 2020.
- [14] F. Lu, H. Zhang, H. Hofmann, and C. Mi, "A double-sided $LCLC$ -compensated capacitive power transfer system for electric vehicle charging," *IEEE Trans. Power Electron.*, vol. 30, no. 11, pp. 6011–6014, Nov. 2015.
- [15] F. Gao, Z. Wang, L. Li, S. Wang, and J. Deng, "Analysis and design of double-sided $LCLC$ compensation parameters with coupling-insensitive ZVS operation for capacitive power transfer," in *Proc. IEEE Energy Convers. Congr. Expo. (ECCE)*, Sep. 2019, pp. 576–581.
- [16] S. Li, Z. Liu, H. Zhao, L. Zhu, C. Shuai, and Z. Chen, "Wireless power transfer by electric field resonance and its application in dynamic charging," *IEEE Trans. Ind. Electron.*, vol. 63, no. 10, pp. 6602–6612, Oct. 2016.
- [17] A. Kumar, S. Sinha, A. Sepahvand, and K. K. Afridi, "Improved design optimization for high-efficiency matching networks," *IEEE Trans. Power Electron.*, vol. 33, no. 1, pp. 37–50, Jan. 2018.
- [18] S. Sinha, A. Kumar, S. Pervaiz, B. Regensburger, and K. K. Afridi, "Design of efficient matching networks for capacitive wireless power transfer systems," in *Proc. IEEE 17th Workshop Control Modeling Power Electron. (COMPEL)*, Jun. 2016, pp. 1–7.
- [19] S. Sinha, A. Kumar, and K. K. Afridi, "Improved design optimization of efficient matching networks for capacitive wireless power transfer systems," in *Proc. IEEE Appl. Power Electron. Conf. Expo. (APEC)*, Mar. 2018, pp. 3167–3173.
- [20] Y.-G. Su, S.-Y. Xie, A. P. Hu, C.-S. Tang, W. Zhou, and L. Huang, "Capacitive power transfer system with a mixed-resonant topology for constant-current multiple-pickup applications," *IEEE Trans. Power Electron.*, vol. 32, no. 11, pp. 8778–8786, Nov. 2017.
- [21] H. Nishiyama and M. Nakamura, "Capacitance of disk capacitors," *IEEE Trans. Compon., Hybrids, Manuf. Technol.*, vol. 16, no. 3, pp. 360–366, May 1993.
- [22] J. Dai and D. C. Ludois, "Capacitive power transfer through a conformal bumper for electric vehicle charging," *IEEE J. Emerg. Sel. Topics Power Electron.*, vol. 4, no. 3, pp. 1015–1025, Sep. 2016.

- [23] *IEEE Standard for Safety Levels With Respect to Human Exposure to Radio Frequency Electromagnetic Fields, 3kHz to 300GHz*, IEEE Standard C95.1-2005, Piscataway, NJ, USA, 2006.
- [24] D. C. Ludois, M. J. Erickson, and J. K. Reed, "Aerodynamic fluid bearings for translational and rotating capacitors in noncontact capacitive power transfer systems," *IEEE Trans. Ind. Appl.*, vol. 50, no. 2, pp. 1025–1033, Mar. 2014.
- [25] R. Mai, B. Luo, Y. Chen, and Z. He, "Double-sided CL compensation topology based component voltage stress optimisation method for capacitive power transfer charging system," *IET Power Electron.*, vol. 11, no. 7, pp. 1153–1160, Jun. 2018.
- [26] M. P. Theodoridis, "Effective capacitive power transfer," *IEEE Trans. Power Electron.*, vol. 27, no. 12, pp. 4906–4913, Dec. 2012.
- [27] J. Lian and X. Qu, "Design of a double-sided LC compensated capacitive power transfer system with capacitor voltage stress optimization," *IEEE Trans. Circuits Syst. II, Exp. Briefs*, vol. 67, no. 4, pp. 715–719, Apr. 2020.
- [28] L. Huang and A. P. Hu, "Defining the mutual coupling of capacitive power transfer for wireless power transfer," *Electron. Lett.*, vol. 51, no. 22, pp. 1806–1807, Oct. 2015.
- [29] S. Y. R. Hui, "Technical and safety challenges in emerging trends of near-field wireless power transfer industrial guidelines," *IEEE Electro-magn. Compat. Mag.*, vol. 7, no. 1, pp. 78–86, 2018.



Jing Lian received the B.Eng. degree in electrical engineering from the China University of Mining and Technology, Xuzhou, China, in 2015. She is currently pursuing the Ph.D. degree in electrical engineering with Southeast University, Nanjing, China.

Her current research interest includes wireless power transfer.



Xiaohui Qu (Senior Member, IEEE) received the B.Eng. and M.Eng. degrees in electrical engineering from the Nanjing University of Aeronautics and Astronautics, Nanjing, China, in 2003 and 2006, respectively, and the Ph.D. degree in power electronics from The Hong Kong Polytechnic University, Hong Kong, in 2010.

From February to May 2009, she was engaged as a Visiting Scholar with the Center for Power Electronics Systems, Virginia Tech, Blacksburg, VA, USA. Since 2010, she has been with the School of Electrical Engineering, Southeast University, Nanjing, where she is currently a Full Professor with a research focus on power electronics. From January 2015 to January 2016, she was a Visiting Scholar with the Center of Reliable Power Electronics (CORPE), Aalborg University, Aalborg, Denmark. Her current research interests include LED lighting systems, wireless power transfer, and power electronics reliability.

Dr. Qu received the Outstanding Reviewer Award and the Prize Paper Award from the IEEE TRANSACTIONS ON POWER ELECTRONICS in 2017 and 2018.



Xi Chen (Senior Member, IEEE) received the B.Eng. degree from Beijing Technology and Business University, Beijing, China, in 2003, the M.Sc. degree from the King's College London, University of London, London, U.K., in 2005, and the Ph.D. degree from The Hong Kong Polytechnic University, Hong Kong, in 2009.

He was a Post-Doctoral Research Fellow with the Institute of Software, Chinese Academy of Sciences, Beijing. He was a Visiting Student with the University of Florida, Gainesville, FL, USA, in 2008.

In 2014, he joined GEIRI North America, San Jose, CA, USA, where he is currently the Chief Information Officer. From 2009 to 2014, he was with State Grid Corporation of China, Beijing. His research interests include nonlinear dynamics, the Internet of Things, smart grids, and electric vehicle charging.

Dr. Chen serves as an Associate Editor for the IEEE SYSTEMS JOURNAL. He served as a Guest Editor of the IEEE TRANSACTIONS ON INTELLIGENT TRANSPORTATION SYSTEMS: Enabling Extreme Fast Charging Technology for Electric Vehicles.



Chunting Chris Mi (Fellow, IEEE) received the B.S.E.E. and M.S.E.E. degrees in electrical engineering from Northwestern Polytechnical University, Xi'an, China, in 1985 and 1988, respectively, and the Ph.D. degree in electrical engineering from the University of Toronto, Toronto, ON, Canada, in 2001.

He was with the University of Michigan–Dearborn, Dearborn, MI, USA, from 2001 to 2015.

He is currently a Professor and the Chair of Electrical and Computer Engineering and the Director of the Center for Electric Drive Transportation, Department of Energy-funded Graduate Automotive Technology Education, San Diego State University (SDSU), San Diego, CA, USA.

Dr. Mi received the Distinguished Teaching Award, the Distinguished Research Award from the University of Michigan–Dearborn, the 2007 IEEE Region 4 Outstanding Engineer Award, the IEEE Southeastern Michigan Section Outstanding Professional Award, and the SAE Environmental Excellence in Transportation (E2T). He has also served as a Panelist in major IEEE and SAE conferences.